Experimental Integrity Evaluation of Tightly-Integrated IMU/LiDAR Including Return-Light Intensity Data

Ali Hassani, Virginia Tech, Blacksburg, VA Nicholas Morris, University of Alabama, Huntsville, AL Matthew Spenko, Illinois Institute of Technology, Chicago, IL Mathieu Joerger, Virginia Tech, Blacksburg, VA

Abstract

This paper describes the design, analysis, and experimental evaluation of a new method to integrate measurements from light detection and ranging (LiDAR) and inertial measurement units (IMU). A tight IMU/LiDAR integration scheme is developed, which aims at exploiting the complementary properties of the two sensors while facilitating safety risk evaluation. In particular, the IMU is used to improve LiDAR position and orientation prediction (or pose), thereby reducing the the risk of incorrectly associating sensed features with mapped landmarks. Conversely, LiDAR pose estimation updates can limit the drift of IMU errors over time. In order to further improve data association, LiDAR return-light intensity measurements are incorporated, which helps distinguish landmarks and thus reduces the risk of incorrect associations. The new method is evaluated and analyzed using experimental data.

1. Introduction

This work is intended for automated driving systems (ADS) applications. In order to quantify safety risks in ADS navigation, this paper leverages prior analytical work in aviation navigation where safety is assessed in terms of integrity. Integrity is a measure of trust in sensor information. The integrity risk is the probability of undetected sensor errors causing unacceptably large positioning uncertainty [1]. Several methods have been established to predict integrity risk in Global Navigation Satellite Systems (GNSS)-based aviation applications [2, 3]. Unfortunately, the same methods do not directly apply to ADS, because ground vehicles operate under sky-obstructed areas where GNSS signals can be altered or blocked by buildings and trees.

ADS require sensors in addition to GNSS, including IMU, LiDARs, cameras, or radars. This paper focuses on IMU and LiDARs. A raw LiDAR scan is made of thousands of data points, each of which individually does not carry useful navigation information. Raw measurements must therefore be processed before they can be used for localization. These processes can include identifying and tracking recognizable, static features in the perceived environment.

The features that we will exploit not only include landmark position, but also surface reflectivity. Previous knowledge of feature parameters can be provided from a landmark map. To estimate the ADS pose starting from a raw laser scan, two intermediary pre-estimator procedures must be carried out: Feature Extraction (FE), and Data Association (DA).

First, FE aims at finding the few most consistently recognizable, viewpoint-invariant landmarks in the raw sensor data. The extracted features must not only be identifiable over repeated observations but must also be distinguishable from one landmark to another. Second, LiDARs provide pose estimation by comparing current-time landmark feature measurements to prior knowledge of these features from the landmark map. DA aims at finding the ordering of mapped landmarks that matches that of sensed, extracted landmarks over successive observations [6, 7]. The incorrect association is a well-known problem that can lead to large navigation errors, thereby representing a threat to navigation integrity.

FE and DA can be challenging in the presence of sensor uncertainty. This is why many sophisticated algorithms have been devised [8-11]. Several publications on multi-target tracking describe relevant approaches to evaluate the probability of correct association in the presence of measurement uncertainty [9, 12-14]. However, these algorithms are not well suited for safety-critical ADS applications due to their lack of prediction capability, to approximations that do not necessarily upperbound risks, and to high computational loads. Also, the risk of FE is not addressed. Overall, research on integrity and continuity of FE and DA is sparse.

This paper builds upon prior work in [15-18], where we developed an analytical integrity risk prediction method for FE and DA. At the FE step, we established a probabilistic normalized separation metric between landmarks, ensuring that they could be reliably, quantifiably distinguished from each other. We then derived a multiple-hypothesis Extended Kalman filter (EKF) innovation-based DA process [16], which provides the means to evaluate the Probability of Incorrect Associations (PIA) while considering all potential measurement combinations and permutations (i.e., all potential incorrect associations). PIA was used to establish a compact expression for the integrity risk of laser-based pose estimation over successive iterations. References [16-17] showed that PIA could quickly grow in the presence of poorly distinguishable landmarks. One approach to mitigate this problem is to select a subset of features sensed by the LiDAR in the environment [18, 19]. But, this approach reduces the number of redundant associations and lowers the ability to detect unwanted, unmapped landmarks [18].

In response, in this paper, we enhance data association and integrity performance by two other means: first, by tightly integrating LiDAR with IMU; second, by incorporating LiDAR return-light intensity measurements. In addition, we design and implement an experimental testbed to statistically evaluate the data association and localization performance of the IMU/LiDAR algorithm.

Integration of LiDAR with IMU can help improve pose prediction and hence increase the success rate of EKF innovation-based data associations. Prior work on IMU/LiDAR integration includes loose and tight coupling schemes primarily aimed at using IMU to coast between LiDAR pose updates and at using LIDAR updates to calibrate IMU biases [20]. One implementation uses the IMU to determine the laser scanner's tilt angle [21-22]. In our previous work [15], we developed a tightly-integrated IMU/LiDAR process specifically to quantify integrity risk. We performed covariance analyses for a two landmark scenario, suggesting IMU integration could reduce integrity risk not only by improving pose estimation but also by reducing the risk of incorrect associations. In this paper, we test this risk quantification algorithm using experimental data.

In parallel to IMU/LiDAR integration, we evaluate a new method to exploit return-light intensity measurements, which LiDARs can provide in addition to range and bearing angle observations. Light intensity measurements can improve the system's ability to distinguish landmarks if the landmark surfaces have different reflectivity properties. For example, LiDAR intensity can help identify an aluminum pole from a pedestrian.

The second section of the paper describes the tightly-integrated IMU/LiDAR algorithm. Non-linear continuous-time process and measurement equations are derived, linearized, and discretized. The third section of the paper is an overview of the multiple-hypothesis DA risk and integrity risk evaluation method [16]. The focus is on the contribution of IMU and LiDAR intensity measurements on the innovation-based DA. The fourth section describes an experimental testbed specifically designed to evaluate navigation integrity risk. In the fifth section of the paper, we present and analyze experimental test results. The reference configuration uses LiDAR range and bearing angles only. We quantify the reduction in integrity risk obtained when incorporating (a) IMU data, (b) LiDAR intensity measurements, and (c) both IMU data and LiDAR intensity.

2. IMU and LiDAR Measurement-Level Integration

2.1 IMU Measurement model

2.1.1 Nonlinear Vehicle Acceleration Equation

IMU accelerometers measure vehicle acceleration with respect to the inertial frame (labeled 'I') and ADS position and orientation are expressed in the navigation frame 'N' (for example, in the East, North, Up directions). We also define the earth frame 'E', which is earth-centered, earth-fixed. The IMU is fixed in the ADS body frame 'B', which can be oriented along the vehicle's maximum moment of inertia axes as described in [21, 22].

We use the Newton and Euler method to describe the ADS translational and rotational motion. The vehicle's velocity and position differentiated with respect to earth frame 'E' and expressed in navigation frame 'N' are written as [23,25]:

$${}^{\mathrm{N}}\dot{\mathbf{v}}_{ADS}^{\mathrm{E}} \equiv \frac{{}^{\mathrm{E}}d{}^{\mathrm{N}}\mathbf{v}_{ADS}^{\mathrm{E}}}{dt} = \mathbf{C}_{\mathrm{B}}^{\mathrm{N}\mathrm{B}}\overline{\mathbf{f}}^{\mathrm{I}} - (2{}^{\mathrm{N}}\boldsymbol{\omega}^{\mathrm{IE}} + {}^{\mathrm{N}}\boldsymbol{\omega}^{\mathrm{EN}}) \times {}^{\mathrm{N}}\mathbf{v}_{ADS}^{\mathrm{E}} + {}^{\mathrm{N}}\mathbf{g}^{\mathrm{E}}$$
(1)

$${}^{\mathrm{N}}\dot{\mathbf{x}}_{ADS}^{\mathrm{E}} \equiv \frac{{}^{\mathrm{E}}d{}^{\mathrm{N}}\mathbf{x}_{ADS}^{\mathrm{E}}}{dt} = {}^{\mathrm{N}}\mathbf{v}_{ADS}^{\mathrm{E}}$$
(2)

The vehicle's Euler angular velocity differentiation can be expressed as [23,26]:

 $\dot{\mathbf{e}}_{ADS} = \mathbf{B}_{\phi \, \theta \, W} \left({}^{\mathrm{B}} \overline{\boldsymbol{\omega}}^{\mathrm{IB}} - \mathbf{C}_{\mathrm{B}}^{\mathrm{N}} \left({}^{\mathrm{N}} \overline{\boldsymbol{\omega}}^{\mathrm{IE}} + {}^{\mathrm{N}} \overline{\boldsymbol{\omega}}^{\mathrm{EN}} \right) \right) \tag{3}$

where

 $^{N}V_{ADS}^{E}$ is the 3×1 vehicle velocity with respect to earth, and expressed in the navigation frame

 $C_{\rm p}^{\rm N}$ is the 3×3 rotation matrix from body frame to navigation frame [23]

 $^{N}\mathbf{x}_{_{ADS}}$ is the 3×1 vehicle position expressed in navigation frame

 ${}^{\rm B}\overline{\bf f}^{\rm I}$ is the 3×1 measured specific force vector at IMU axis center w.r.t. frame I expressed in B [23]

 ${}^{\rm N}\omega^{\rm IE}$ is the angular velocity vector of frame E w.r.t frame I expressed in N

 ${}^{N}\omega^{EN}$ is the angular velocity vector of frame N w.r.t frame E expressed in N

 ${}^{\mathrm{B}}\bar{\omega}^{\mathrm{B}}$ is the meausred angular velocity vector of frame B w.r.t frame I expressed in B

^N**g**^E is the local gravity vector at IMU axis center w.r.t frame E expressed in N [23, 24].

 $[\mathbf{a} \times]$ is the skew-symmetric matrix of vector \mathbf{a} .

 $\mathbf{B}_{4.0}$ is the 3×3 coefficient matrix defined in Appendix A.

Discrete-time forms of equations (1-3) can be found in Appendix B.

2.1.2 Vehicle Angular Velocity Measurement Equation

An IMU provides a measurement of the angular velocity vector ${}^{B}\omega^{IB}$ of the sensor's body frame 'B' with respect to 'I' expressed in frame B. The following equations are used to model the continuous-time form of the errors impacting the IMU angular velocity measurement. The IMU's measurement of ${}^{B}\omega^{IB}$ can be expressed as:

$${}^{\mathrm{B}}\tilde{\boldsymbol{\omega}}^{\mathrm{IB}} = \left[\mathbf{I} + \mathbf{S}_{\varrho} + \mathbf{M}_{\varrho}\right] {}^{\mathrm{B}}\boldsymbol{\omega}^{\mathrm{IB}} + \mathbf{b}_{\varrho} + \mathbf{v}_{\varrho} \tag{4}$$

where

 $^{\mathrm{B}}\omega^{\mathrm{IB}}$ is the 3×1 true angular velocity vector of body B with respect to I expressed in body frame B

 ${}^{\mathrm{B}}\tilde{\omega}^{\mathrm{IB}}$ is the measured angular velocity vector of body B with respect to I expressed in B

 S_{σ} and M_{σ} are the actual gyroscope scale factor and misalignment matrices in B

 \mathbf{b}_{g} is the gyroscope time-varying bias vector in B

 $\mathbf{v}_{_{\sigma}}$ is gyroscope measurement white noise error component expressed in B

2.1.3 IMU Sensor Error Model

Equation (4) expresses the fact that the gyroscope scale factor and misalignment matrices (\mathbf{S}_g and \mathbf{M}_g) affect the measured angular velocity $^B\tilde{\boldsymbol{\omega}}^{IB}$. Scale factor and misalignment errors are corrected to obtain $^B\bar{\boldsymbol{\omega}}^{IB}$, which is the vector used in practice as gyroscope output.

$${}^{\mathrm{B}}\overline{\boldsymbol{\omega}}^{\mathrm{IB}} = \left[\mathbf{I} + \hat{\mathbf{S}}_{g} + \hat{\mathbf{M}}_{g}\right]^{-1} \left({}^{\mathrm{B}}\widetilde{\boldsymbol{\omega}}^{\mathrm{IB}} - \hat{\mathbf{b}}_{g}\right)$$
 (5)

where

 $\hat{\mathbf{S}}_{\sigma}$ and $\hat{\mathbf{M}}_{\sigma}$ are the estimated gyroscope scale factor and misalignment matrices in B

 $\hat{\mathbf{b}}_{\sigma}$ is the estimated gyroscope time-varying bias vector in B

The time-varying part of the gyroscope bias \mathbf{b}_g can be modeled as a first order Gauss Markov Random Process (GMRP) [20, 24], and the continuous-time GMP equation can be written as:

$$\dot{\mathbf{b}}_{g} = -\frac{1}{\tau_{g}} \mathbf{b}_{g} + \mathbf{n}_{g} \tag{6}$$

where

 τ_g is the GMP time constant

 \mathbf{n}_g is a 3×1 vector of GMP time-uncorrelated driving noise

The discrete-time form of equations (4) to (6) are provided in Appendix B [23]. In equations (4) to (6), subscript 'g' stands for 'gyroscope'. We can write similar equations for the specific force vector of the body frame with respect to the inertial frame ${}^{B}\tilde{\mathbf{f}}^{1}$ which is measured by accelerometers (subscript 'a').

$${}^{\mathrm{B}}\tilde{\mathbf{f}}^{\mathrm{I}} = [\mathbf{I} + \mathbf{S}_{a} + \mathbf{M}_{a}] {}^{\mathrm{B}}\mathbf{f}^{\mathrm{I}} + \mathbf{b}_{a} + \mathbf{v}_{a}$$
 (7)

$${}^{\mathbf{B}}\mathbf{\bar{f}}^{\mathbf{I}} = [\mathbf{I} + \hat{\mathbf{S}}_{a} + \hat{\mathbf{M}}_{a}]^{-1} ({}^{\mathbf{B}}\mathbf{\tilde{f}}^{\mathbf{I}} - \hat{\mathbf{b}}_{a})$$

$$(8)$$

$$\dot{\mathbf{b}}_{a} = -\frac{1}{\tau_{a}}\mathbf{b}_{a} + \mathbf{n}_{a} \tag{9}$$

2.1.4 Linearized IMU Equations

The IMU state parameters include ADS position, velocity, orientation, and IMU biases. The continuous-time model is linearized using a first order Taylor series expansion about reference state parameter values [6]. We use the notation ' δ ' to indicate deviations of state parameters relative to the reference values. Using IMU measurement error equations (5) and (8) and gyro and accelerometer bias equations (6) and (9), we can write a continuous-time linearized state propagation model as [7]:

$$\delta \dot{\mathbf{x}} = \mathbf{F} \ \delta \mathbf{x} + \delta \mathbf{w} \tag{10}$$

$$\delta \mathbf{x} = [\delta \mathbf{x}_{ADS}^{T} \quad \delta \mathbf{v}_{ADS}^{T} \quad \delta \mathbf{e}_{ADS}^{T} \quad \delta \mathbf{b}_{g}^{T} \quad \delta \mathbf{b}_{a}^{T}]$$
(11)

$$\mathbf{F} = \begin{bmatrix} \mathbf{0} & \mathbf{I} & \mathbf{0} & \mathbf{0} & \mathbf{0} \\ \mathbf{F}_{H2V} & \mathbf{0} & \begin{bmatrix} {}^{N}\overline{\mathbf{f}}{}^{1} \times \end{bmatrix} & \mathbf{0} & \mathbf{C}_{B}^{N} \\ \mathbf{0} & \mathbf{F}_{V2T} & -\begin{bmatrix} {}^{N}\boldsymbol{\omega}^{IN} \times \end{bmatrix} & -\mathbf{C}_{B}^{N} & \mathbf{0} \\ \mathbf{0} & \mathbf{0} & \mathbf{0} & -\tau_{a}^{-1}\mathbf{I} & \mathbf{0} \\ \mathbf{0} & \mathbf{0} & \mathbf{0} & \mathbf{0} & -\tau_{a}^{-1}\mathbf{I} \end{bmatrix}, \quad \delta \mathbf{w} = \begin{bmatrix} \mathbf{0} \\ \mathbf{C}_{B}^{N}(-\delta \mathbf{S}_{a}^{B}\overline{\mathbf{f}}^{1} - \delta \mathbf{M}_{a}^{B}\overline{\mathbf{f}}^{1} - \mathbf{v}_{a}) \\ -\mathbf{C}_{B}^{N}(-\delta \mathbf{S}_{g}^{B}\overline{\boldsymbol{\omega}}^{IB} - \delta \mathbf{M}_{g}^{B}\overline{\boldsymbol{\omega}}^{IB} - \mathbf{v}_{g}) \\ \overline{\mathbf{n}}_{g} \\ \overline{\mathbf{n}}_{a} \end{bmatrix}$$
(12)

where

 \mathbf{F}_{V2T} and \mathbf{F}_{H2V} are defined in Appendix A.

 ${}^{N}\omega^{IN}$ is the angular velocity vector of frame I with respect to frame N expressed in frame N; we have ${}^{N}\omega^{IN} = {}^{N}\omega^{IE} + {}^{N}\omega^{EN}$.

 ${}^{\rm N}\overline{\bf f}^{\rm I}$ is the estimated specific force expressed in navigation frame.

The discrete-time form of equation (10) is provided in Appendix B. It can be expressed as:

$$\delta \mathbf{x}_{k+1} = \mathbf{\Phi}_k \delta \mathbf{x}_k + \delta \mathbf{w}_k \tag{13}$$

where Φ_k is the state transition matrix between time step k and k+1.

2.2 LiDAR Feature Extraction Measurement Model

A LiDAR provides a cloud of points in the sensor's frame. The point cloud is a representation of the environment that must be interpreted for navigation. FE aims at determining consistently identifiable landmark features. Figure 1 shows an example LiDAR point cloud collected in our experimental testbed. The testbed includes easy-to-distinguish static vertical cylinders serving as landmarks to facilitate feature extraction (FE). FE is not the primary focus of the paper. The color code represents return light intensity measurements: red is a high-intensity data-point, blue is low intensity.

Figure 2 illustrates the three-step FE algorithm implemented to extract landmark information from LiDAR point clouds. In this paper, FE aims at finding the center of quasi-circular ellipses formed by the projection of vertical cylinders in the LiDAR's zero-elevation plane. (1) *Segmentation*: We use the predicted vehicle pose to place the LiDAR in the landmark map and segment the data in point sets corresponding to cylinders. (2) *Model-Fitting*: We then project each point set in the LiDAR zero-elevation plane and fit a circle through each point set. (3) *Feature Parameter Estimation*: The center of the best-fit circle is the extracted point-feature, which we identify by range and bearing angle with respect to the LiDAR.

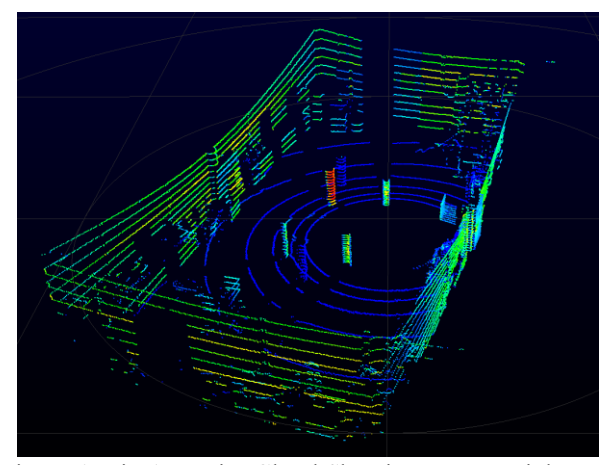


Figure 1. LiDAR Point Cloud Showing Return-Light Intensity (color-coded from blue to red, from low intensity to high intensity).

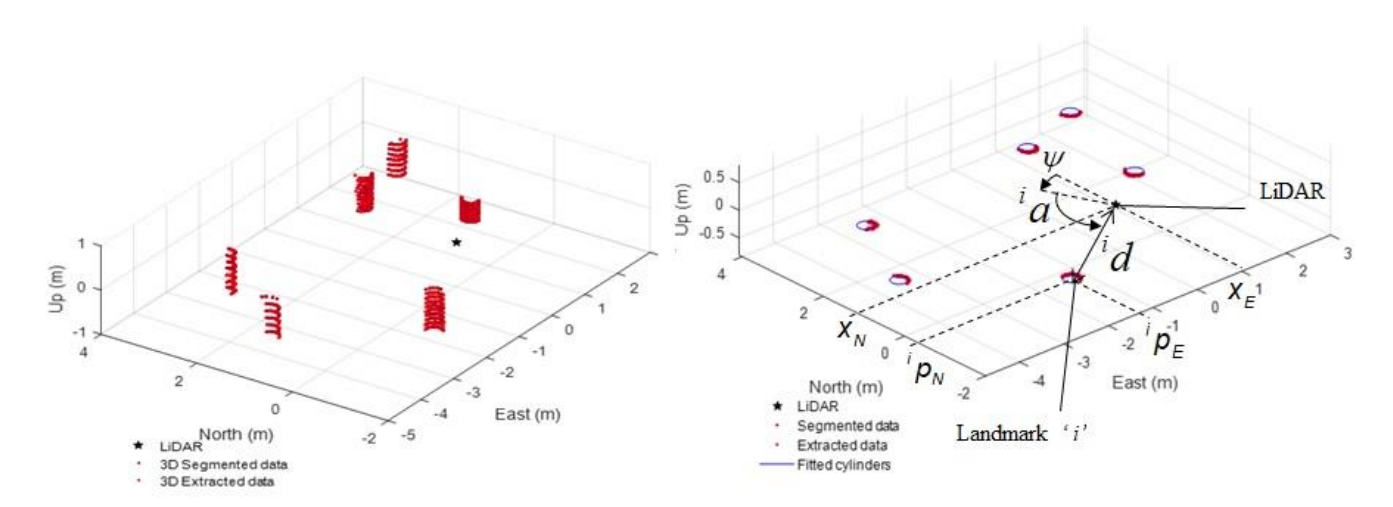


Figure 2. (a) 3D Segmentation of LiDAR Point cloud - (b) Circle Fitting and Point-Feature Measurement Extraction

The following derivation is to express the extracted point-feature range and bearing angle measurement equations. First, let n_L be the number of extracted landmarks. We define id and id as the range and bearing angle measurements in LiDAR frame for landmark i, for i ranging from 1 to n_L . In the landmark map's navigation frame, the horizontal position of the cylinder's center is time-invariant. Its cartersian East and North coordinates are noted ip_E and ip_R for landmark i. In parallel, parameters in our IMU/LiDAR state space realization include the ADS position \mathbf{x}_{ADS} and orientation \mathbf{e}_{ADS} in navigation frame (also appearing in the state error equation (11)), which are expressed as:

$$\overline{\mathbf{x}}_{ADS} = \begin{bmatrix} x_E & x_N & x_U \end{bmatrix}^T \tag{14}$$

$$\overline{\mathbf{e}}_{ADS} = \begin{bmatrix} \phi & \theta & \psi \end{bmatrix}^T \tag{15}$$

The non-linear LiDAR range and angular measurements are respectively given by:

$${}^{i}d = \sqrt{({}^{i}p_{E} - x_{E})^{2} + ({}^{i}p_{N} - x_{N})^{2}} + \nu_{d}$$
(16)

$$^{i}a = \arctan\left(\frac{^{i}p_{N} - x_{N}}{^{i}p_{E} - x_{E}}\right) - \psi + \upsilon_{a}$$

$$\tag{17}$$

where v_d and v_a are random feature measurement errors. In Appendix C, we show that the distributions of v_d and v_a are not Gaussian, but can be overbounded (in the CDF-sense [4,5]) by zero-mean normal distributions. We use the overbounding distributions to model feature parameter measurement uncertainty. We can stack range and bearing measurements for all visible landmarks to obtain the following $2n_I \times 1$ nonlinear LiDAR measurement equation:

$$\hat{\mathbf{z}}_k = \mathbf{h}_{0,k}(\mathbf{x}_k) + \mathbf{v}_k \tag{18}$$

$$\hat{\mathbf{z}}_k = [d_1 \quad \cdots \quad d_{n_L} \quad a_1 \quad \cdots \quad a_{n_L}]^T \tag{19}$$

$$\mathbf{v}_{k} = [\upsilon_{d_{1}} \quad \cdots \quad \upsilon_{d_{n_{t}}} \quad \upsilon_{d_{1}} \quad \cdots \quad \upsilon_{d_{n_{t}}}]^{T} \tag{20}$$

where

 \mathbf{x}_k is the state vector whose corresponding state error vector is defined in equation (11)

 \mathbf{v}_k is the $2n_L \times 1$ feature measurement error vector modeled as a vector of normally distributed random variables with zero mean and covariance matrix \mathbf{V}_k . We use the notation: $\mathbf{v}_k \sim \mathrm{N}(\mathbf{0}, \ \mathbf{V}_k)$.

In equation (18), the subscript 0 indicates that measurements $({}^{i}d, {}^{i}a)$ are correctly matched with the corresponding landmark parameters $({}^{i}p_{E}, {}^{i}p_{N})$. We can linearize equation (18) about our best prediction of the vehicle and landmark positions. The resulting linearized range and angular measurement and measurement error vectors are respectively noted $\delta \mathbf{d}$, $\delta \mathbf{a}$ and \mathbf{v}_{d} , \mathbf{v}_{a} . The linearized LiDAR measurement equation can be written as:

$$\begin{bmatrix} \delta \mathbf{d} \\ \delta \mathbf{a} \end{bmatrix}_{k} = \begin{bmatrix} \mathbf{F}_{d,x} & \mathbf{0} & \mathbf{0} & \mathbf{0} & \mathbf{0} \\ \mathbf{F}_{a,x} & \mathbf{0} & -\mathbf{F}_{a,e} & \mathbf{0} & \mathbf{0} \end{bmatrix}_{k} \begin{bmatrix} \delta \mathbf{x}_{ADS} \\ \delta \mathbf{v}_{ADS} \\ \delta \mathbf{e}_{ADS} \\ \delta \mathbf{b}_{g} \\ \delta \mathbf{b}_{a} \end{bmatrix}_{k} + \begin{bmatrix} \mathbf{v}_{d} \\ \mathbf{v}_{a} \end{bmatrix}_{k}$$
(21)

where the coefficient matrices $\mathbf{F}_{d,x}$, $\mathbf{F}_{a,x}$ and $\mathbf{F}_{a,e}$ are determined using the state prediction vector and assuming correct association as described in Appendix A.

Let n_F be the number of extracted feature measurements per landmark ($n_F = 2$ for the LiDAR's angular and ranging measurements), and let n_L be the number of visible landmarks. The total number of extracted feature measurements is $n \equiv n_L n_F$. Let $\hat{\mathbf{z}}_k$ be the $n \times 1$ feature measurement vector in (18). We use the analysis in Appendix C to model $\hat{\mathbf{z}}_k$ as: $\hat{\mathbf{z}}_k \sim N(\mathbf{z}_k, \mathbf{V}_k)$. Equation (21) can be re-written in terms of the predicted state vector $\overline{\mathbf{x}}_k$ under the correct association hypothesis (subscript 0) as:

$$\hat{\mathbf{z}}_{k} - \mathbf{h}_{0k}(\overline{\mathbf{x}}_{k}) = \mathbf{H}_{k} \delta \mathbf{x}_{k} + \mathbf{v}_{k} \tag{22}$$

where the observation matrix \mathbf{H}_k is the measurement-to-state coefficient matrix given in equation (21) [28].

In addition to range and bearing angle measurements, LiDAR provides intensity measurements for each point in the cloud. We obtain a mean intensity measurement for landmark 'i' by averaging intensity values for all points in a point set associated with landmark i. The $n_L \times 1$ return-light intensity measurement vector is defined as:

$$\hat{\mathbf{s}}_k = \mathbf{s}_k + \mathbf{v}_{s,k} \tag{23}$$

We assume that $\hat{\mathbf{s}}_k$ is normally distributed with mean \mathbf{s}_k and covariance matrix $\mathbf{V}_{s,k}$. We use the notation: $\hat{\mathbf{s}}_k \sim \mathrm{N}(\mathbf{s}_k \ , \ \mathbf{V}_{s,k})$. \mathbf{s}_k is the vector of true mean landmark intensity. Vector $\mathbf{v}_{s,k}$ is an $n_L \times 1$ intensity measurement error vector modeled as $\mathbf{v}_{s,k} \sim \mathrm{N}(\mathbf{0}, \ \mathbf{V}_{s,k})$. Equation (22) and (21) are the LiDAR's linearized extracted feature measurements.

3. Integrity Risk Evaluation Considering Correct and Incorrect Data Association

3.1 EKF-Based Vehicle State Estimation using IMU/LiDAR

We use an EKF to predict using IMU in equation (13) and to estimate using LiDAR in equation (22) the state vector \mathbf{x}_k . The LiDAR linearized measurement equation is used to get a correction $\delta \mathbf{x}_k$, hence, an estimate $\hat{\mathbf{x}}_k = \overline{\mathbf{x}}_k + \delta \mathbf{x}_k$ of the ADS state vector and covariance matrix $\hat{\mathbf{P}}_k$ [27].

In order to analyze the impact of incorporating IMU and LiDAR intensity measurements, we will consider four configurations: LiDAR-only, IMU/LiDAR, LiDAR with intensity measurements, which we label 'LiDAR+', and 'IMU/LiDAR+' that incorporates all available sensor information. When using LiDAR only, state prediction $\bar{\mathbf{x}}_k$ is obtained using a coarse kinematic model to replace equation (13). This model propagates ADS states assuming a constant velocity vector between LiDAR measurement updates. This can be inaccurate for high ADS dynamics or if a LiDAR update is skipped. When using the IMU, we use equation (13) improve state prediction $\bar{\mathbf{x}}_k$, but also to enhance data association.

This paper makes two contributions to previous association risk evaluation methods in [15]. First, we devise a process to handle unexpectedly un-extracted landmarks or extracted-but-unmapped landmarks, which can occur if an obstacle moves into the LiDAR field of view. Second, we derive a method to incorporate LiDAR return-light intensity in data association.

3.2 Innovation-Based Data Association

To perform data association, we use an innovation-based approach [12]. The innovation vector $\gamma_{0,k}$ under correct association is given by [29]:

$$\mathbf{\gamma}_{0k} \equiv \hat{\mathbf{z}}_k - \mathbf{h}_{0k}(\overline{\mathbf{x}}_k) \tag{24}$$

The innovation vector can be interpreted as a measure of consistency between LiDAR extracted feature measurements and state prediction. Thus, the more accurate state prediction is (and it is more accurate using IMU), the more efficient the data association process becomes.

3.2.1 Handling Landmarks Unexpectedly Coming In and Out of View of the LiDAR

Extracted range and bearing measurements are arranged landmark-by-landmark in an arbitrary order in vector $\hat{\mathbf{z}}_k$ at time k. In this paper, we account for incorrect associations even in the case where the number of perceived landmarks differs from the number of mapped landmarks. Let n_L be the number of visible landmarks, and n_M be the number of landmarks that are expected to be visible according to LiDAR pose prediction in the landmark map (the term pose designates position and orientation). For example, if $n_M > n_L$, then there are $C(n_M, n_L) \equiv n_M!/((n_M - n_L)! n_L!)$ possible combinations of perceived landmarks with mapped ones. In general, the number of subsets (or landmark combinations) to be considered is $h_C \equiv C(\max\{n_L, n_M\}, \min\{n_L, n_M\})$.

In addition, within each subset of $\min\{n_L, n_M\}$ landmarks, there are different ways that 'mapped versus perceived' landmarks can be associated [16]. There are $h_P \equiv (\min\{n_L, n_M\}!)$ potential ways for assigning observed with mapped landmarks, which is the number of possible landmark permutations.

Incorrect association (IA) occurs when the ordering of measured landmarks differs from that of mapped landmarks assumed in the EKF. There can only be one correctly matched 'mapped versus perceived' landmark subset, so that the number of IA is: $h_{IA} \equiv h_C h_P - 1$. For risk evaluation, we consider all possible subset orderings of measurements $\overline{\mathbf{z}}_{i,k} = \mathbf{h}_{i,k}(\overline{\mathbf{x}}_k)$ and $\mathbf{s}_{i,k}$ where $i = 0,...,h_{IA}$. Subscripts zero indicate the correct association.

The table 1 represents an example scenario where $n_L = 3$ landmarks are extracted from the LiDAR (labeled 1, 2, 3), and $n_M = 3$ landmarks are predicted to be seen using the map (labeled A, B, C). The number of landmark subsets to be considered is $h_C = 1$, and the number of possible landmark permutations is $h_P = 6$, so that $h_L = 5$ IAs are possible. Table 2 shows another scenario where $n_L = 2$, and $n_M = 3$. In this case, $h_C = 3$, and $h_P = 2$, so that $h_L = 5$ IAs are possible.

Table 1. 1st Example Scenario, 3 Extracted vs 3 Mapped Landmarks Association

	[1 2 3]
CA	[A B C]
IA	[A C B]
	[B A C]
	[B C A]
	[C A B]
	[C B A]

Table 2. 2nd Example Scenario, 2 Extracted vs 3 Mapped Landmarks Association

	[1 2 Ø]
CA	[A B C]
IA	[B A C]
	[A C B]
	[C A B]
	[B C A]
	[C B A]

The innovation vector $\mathbf{\gamma}_{i,k}$ is zero mean only under correct association. Any other (incorrect) association causes the mean of the innovation vector to be non-zero. Thus, the innovation vector is a good indicator of incorrect association. The innovation vector can be expressed as:

$$\mathbf{\gamma}_{i,k} = \hat{\mathbf{z}}_k - \mathbf{A}_{i,k} \mathbf{C}_{i,k} \mathbf{h}_{0,k} (\overline{\mathbf{x}}_k) \tag{25}$$

where

$$\mathbf{y}_{i,k} \equiv \mathbf{B}_{i,k} \mathbf{h}_{0,k} (\mathbf{x}_k) \quad , \quad \mathbf{B}_{i,k} \equiv \mathbf{A}_{0,k} \mathbf{C}_{0,k} - \mathbf{A}_{i,k} \mathbf{C}_{i,k} \quad , \quad \mathbf{y}_{0,k} = \mathbf{0}$$
 (26)

and where $\mathbf{A}_{i,k}$ are $n \times n$ permutation matrices of n_F -dimensional blocks, and $\mathbf{C}_{i,k}$ are $n \times (\min\{n_M, n_P\}n_F)$ combination matrices (also for combinations of n_F -dimensional blocks) for $i = 0,...,h_M$. The state prediction vector $\overline{\mathbf{x}}_k$ in equations (24) and (25) is more accurate using an IMU than using an ADS kinematic model. We leverage this fact to reduce the risk of incorrect associations using IMU data.

The ordering of mapped landmarks that minimizes weighted norm of the innovation vector can be used to identify correct association [29]. Based on this criterion, we define the minimum separation distance as:

$$\gamma_k^2 = \min_{i=0, h, L} \left\| \mathbf{\gamma}_{i,k} \right\|_{\mathbf{Y}_{i,k}}^2 \quad \text{where} \quad \left\| \mathbf{\gamma}_{i,k} \right\|_{\mathbf{Y}_{i,k}}^2 \equiv \mathbf{\gamma}_{i,k}^T \mathbf{Y}_{i,k}^{-1} \mathbf{\gamma}_{i,k} \quad \text{and} \quad \mathbf{Y}_{i,k} \equiv \mathbf{A}_{i,k} \mathbf{C}_{i,k} \mathbf{H}_k \overline{\mathbf{P}}_k \mathbf{H}_k^T \mathbf{C}_{i,k}^T \mathbf{A}_{i,k}^T + \mathbf{V}_k$$
 (27)

3.2.2 Incorporating LiDAR Return-Light Intensity to Improve Association

In addition, comparing the landmarks LiDAR-extracted mean intensity measurements to values in the map improves data association. We first define the intensity-separation vector as the difference between the LiDAR extracted intensity measurement and the mean of each landmark intensity as stored in the landmark map. The intensity-separation vector $\xi_{i,k}$ can be expressed as:

$$\boldsymbol{\xi}_{i,k} = \hat{\boldsymbol{s}}_k - \overline{\boldsymbol{s}}_{i,k} \quad , \quad \boldsymbol{\xi}_{i,k} \sim N(\boldsymbol{s}_k, \ \boldsymbol{A}_{S,i,k} \boldsymbol{C}_{S,i,k} \overline{\boldsymbol{S}}_k \boldsymbol{C}_{S,i,k}^T \boldsymbol{A}_{S,i,k}^T + \boldsymbol{V}_{S,k})$$
(28)

where

 \mathbf{s}_{k} is the true value of the mean return-light intensity

 $\hat{\mathbf{s}}_k$ is the LiDAR's measured mean return-light intensity for all n_L visible landmarks; we assume: $\hat{\mathbf{s}}_k \sim N(\mathbf{s}_k, \mathbf{V}_{S,k})$

 $\overline{\mathbf{s}}_{i,k}$ is the mapped mean return-light intensity for the n_M expected landmarks under the i^{th} association hypothesis;

 \overline{S}_k is the $n_M \times n_M$ covariance matrix capturing the uncertainty in mapped landmark's mean light intensity values

 $\mathbf{A}_{s_{i,k}}$ are $n_L \times n_L$ permutation matrices similar to the ones in equation (27) but for scalar permutations, for $i = 0,...,h_M$

 $\mathbf{C}_{s,i,k}$ are $n_L \times n_M$ scalar combination matrices for $i = 0,...,h_M$

Similar to the innovation vector in equation (24), the intensity separation vector in equation (28) is zero mean only if the correct association is found. Landmark intensity parameters are not included in the EKF because they do not provide direct information on ADS states. Still, we can improve the association criterion by augmenting the innovation vector with $\xi_{i,k}$. The resulting 'separation vector' is defined as: $\zeta_{i,k} = [\gamma_{i,k}^T \quad \xi_{i,k}^T]^T$. The minimum norm of the separation vector weighted by its covariance matrix, which we referred to as the 'separation', is defined as:

$$\zeta_{k}^{2} = \min_{i=0,\dots,h_{L}} \left\| \zeta_{i,k} \right\|_{\mathbf{Z}_{i,k}^{-1}}^{2} \quad \text{where} \quad \mathbf{Z}_{i,k} = \begin{bmatrix} \mathbf{A}_{i,k} \mathbf{C}_{i,k} \mathbf{H}_{k} \mathbf{\bar{P}}_{k} \mathbf{H}_{k}^{T} \mathbf{C}_{i,k}^{T} \mathbf{A}_{i,k}^{T} + \mathbf{V}_{k} & \mathbf{0} \\ \mathbf{0} & \mathbf{A}_{s\,i,k} \mathbf{\bar{S}}_{k} \mathbf{C}_{s\,i,k}^{T} \mathbf{\bar{A}}_{s\,i,k}^{T} + \mathbf{V}_{s,k} \end{bmatrix}$$
(29)

3.3 Integrity Risk equation

The integrity risk $P(HMI_k)$ or probability of hazardously misleading information (HMI) is the probability of the ADS being outside of a specified alert limit box when the vehicle position is estimated to be inside this box [4-6]. In ADS lane centering applications, lateral deviations are of primary concern and the alert limit can be defined as the distance between the edge of the car and the edge of the lane when the car is at the center of the lane [4-6, 16, 30]. An analytical bound on the integrity risk that considers all possible incorrect associations is given in [29], and can be expressed as:

$$P(HMI_{k}) \le 1 - \left[1 - P(HMI_{k} \mid CA_{K})\right] \prod_{j=1}^{k} P(CA_{j} \mid CA_{J-1}) + I_{ALLOC,k}$$
(30)

with

$$P(HMI_k \mid CA_K) = Q(\ell/\sigma_k) + 1 - Q(-\ell/\sigma_k)$$
(31)

$$P(CA_j \mid CA_{J-1}) \ge 1 - P\left(q_j^2 \ge \min_{i=1,\dots,h_n,h_r} \left\{L_{i,j}^2/4\right\}\right)$$
(32)

where

K designates a range of time indices: $K = \{0,...k\}$

Q() is the tail probability function of the standard normal distribution

 ℓ is the specified alert limit that defines a hazardous situation

 σ_k is the standard deviation of the estimation error for the vehicle state of interest

 $I_{REO,k}$ is the overall integrity risk requirement

 $I_{ALLOC,k}$ is a predefined integrity risk allocation at FE, chosen to be a small fraction of $I_{REO,k}$.

 q_j^2 is a chi-square distributed random variable with a number of degrees of freedom that is the sum of the number of measurements and of states at time step j

 $L_{i,j}^2$ can be determined at FE, and represents the minimum value of the mean landmark feature separation at DA i and time step j. [29]

The probability of correct association in equation (32) is a function of $L_{i,j}^2$, which defines a probabilistic lower bound on the true value of ζ_k in equation (29). This lower-bound on landmark separation is set such that the risk of the true value of ζ_k being smaller than $L_{i,j}^2$ does not exceed $I_{ALLOC,k}$.

In this section, by integrating LiDAR with IMU, we can reduce positioning errors, thereby lowering the risk $P(HMI_k \mid CA_K)$. In addition, IMU measurements are instrumental in improving state prediction, thereby increasing the ability to distinguish landmarks. In the equations, IMU measurements enable increased values of $L_{i,j}^2$, which increases the probability of correct association $P(CA_j \mid CA_{J-1})$ and ultimately reduces $P(HMI_k)$. Incorporating LiDAR return light intensity has the same effect, which we quantify using experimental data in the next section.

4. Experimental Testbed

We have designed and built an experimental testbed specifically to quantify the risk of incorrect association and $P(HMI_k)$. This testbed pictured Figure 3 is composed of a rover on a figure-eight track, which houses a sensor platform. The rover can operate for many hours unattended to collect LiDAR and IMU data over repeated trajectories. The sensor platform mounted on the rover includes the LiDAR and the IMU stacked vertically in order to minimize lever arms and misalignments between their sensor frames. In addition, an infrared (IR) camera motion capture system (by VICON) provides truth trajectory tracking measurements. IR markers are fixed on the rover and LiDAR sensor.

In this experiment, cardboard cylinders serve as landmarks for ease of FE from LiDAR point clouds. They are covered with white and black felts and retro-reflective straps to provide different surface reflectivity. IR markers are placed around

the edge of the cylinders for surveying using IR cameras. One of the landmarks will periodically be occluded behind another one, which will test the data association process' ability to dynamically distinguish landmarks.

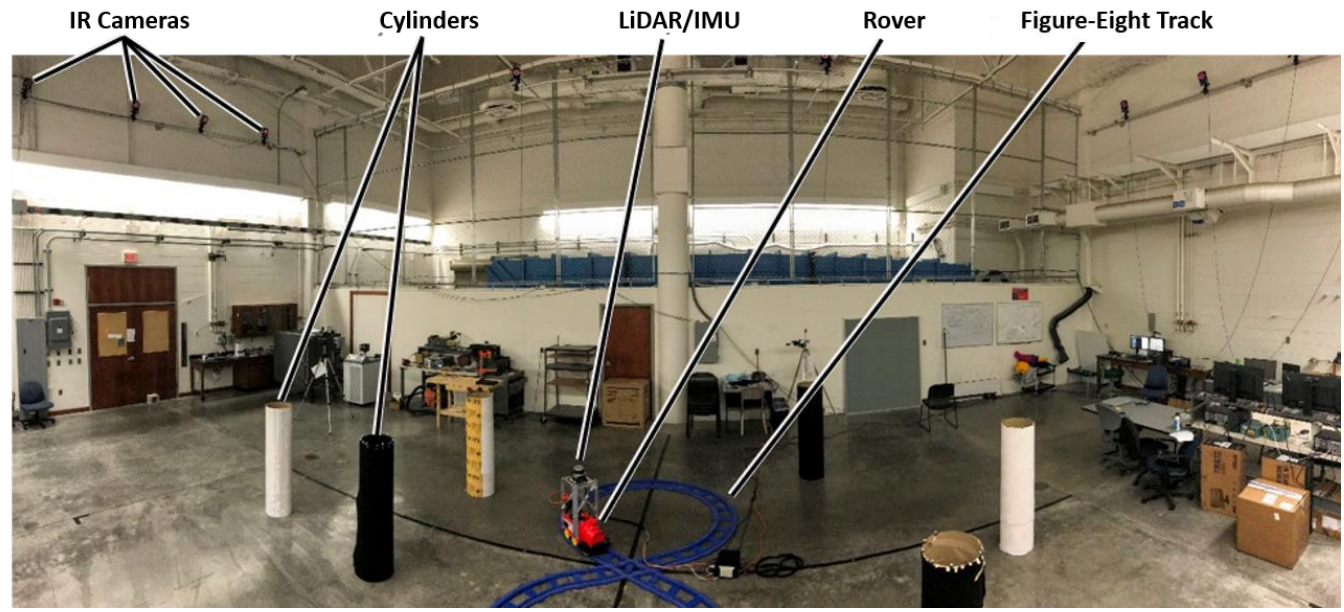


Figure 3. Testbed set up

IR cameras (shown in Figure 4) provide truth values for the position and orientation of the LiDAR and IMU sensors in the navigation frame. They are also used to map landmark locations. Twelve cameras, four VICON MX-T20s and eight Vantage 5s, record small retro-reflective markers placed on the sensors and landmarks, providing sub-centimeter level positioning. We also use a Velodyne's VLP-16 Puck LTE LiDAR and a NovAtel's IMU-IGM-A1 coupled with NovAtel's ProPak6. The IMU is set to record at 100 Hz sampling rate. The IR cameras data set is used as true values to determine errors in multi-sensor ADS trajectory estimation. All three sensors, IR cameras, LiDAR, and IMU, are time-tagged using the same computer clock.

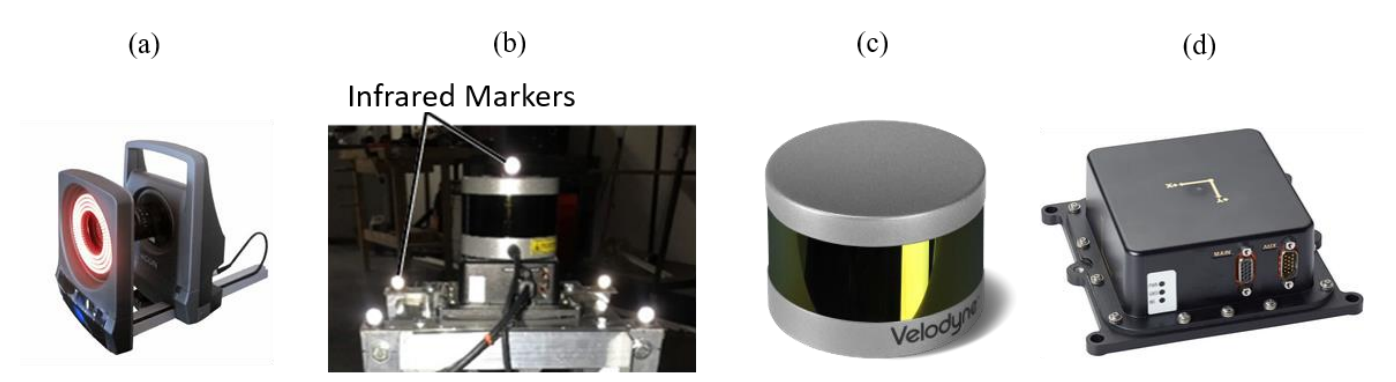


Figure 4. (a) IR camera; (b) IR markers on sensor platform; (c) LiDAR -VLP-16 Puck; (d) IMU-IGM-A1

5. Navigation Performance Test Results Using LiDAR

In this section, we quantify navigation integrity for the multi-sensor IMU/LiDAR system described in Section 4. As aanounced in Section 3.1, we consider four configurations: LiDAR-only, IMU/LiDAR, LiDAR+ (i.e., incorporating mean intensity measurements to LiDAR range and bearing angle), and 'IMU/LiDAR+' (using all available sensor information). We perform four tests to quantify risk reductions brought about by incorporating IMU and LiDAR intensity measurements as compared to LiDAR-only. In each test, the rover is moving on a figure-eight track next to a predefined set of landmarks, some of which may be occluded over segments of the trajectory. The four tests can be described as follows.

- $Test\ 1 LiDAR-only$: We only use LiDAR range and bearing measurements.
- Test 2 IMU/LiDAR: The IMU data is incorporated with LiDAR range and bearing measurements. We artificially impose a limit on LiDAR range measurements.
- Test 3 LiDAR+: The LiDAR intensity measurement is incorporated with LiDAR range and bearing measurements. Landmark occlusions occur causing high risk of incorrect association.
- Test 4 IMU/LiDAR+: LiDAR range, bearing and intensity data are incorporated with IMU data.

Table 3 lists parameters and settings which are common to all tests. We use two landmarks in Tests 1-2 and four landmarks in Tests 3-4. Each landmark is identified by a number ranging from 1 to 4. In Tests 3 and 4, landmark surface properties are not all the same: we use cylinders with black surfaces (labeled 'B' on figures), white surfaces ('W') and retro-reflective surfaces ('RR'). The nominal LiDAR range limit is set to 10 meters in Tests 1, 3, 4, and reduced to 4 meters in Test 2.

Table 3	Common	settings	and	Parameters
raute 5.	Common	SCHIIIZS	anu	1 ar arricults

System Parameters	Values
standard deviation of feature extraction ranging measurement	0.15 m
standard deviation of feature extraction angular measurement	3 deg
Laser data sampling interval	0.1 s
Vehicle speed	0.6 m/s
Alert limit ℓ [7]	0.35 m

5.1 Using LiDAR Range and Bearing Angle Measurements

In this 'LiDAR-only' implementation, we use LiDAR ranging and bearing angle measurements. Two black-colored landmarks (labeled 1 and 2) are in view of the 360 degree-azimuth LiDAR as shown in Figure 5. The LiDAR range limit is such that all landmarks are continuously in view of the LiDAR. The estimated trajectory is represented with a blue line and the true trajectory with a black line. Estimated and true trajectories are overlapping. The black arrow shows the direction of motion at the starting point. Background colors will help identify segments of the rover trajectory when presenting results over time: the rover follows straight line paths in the dark gray area, is in the top loop when in the white area, and in the bottom loop when in the light gray area.

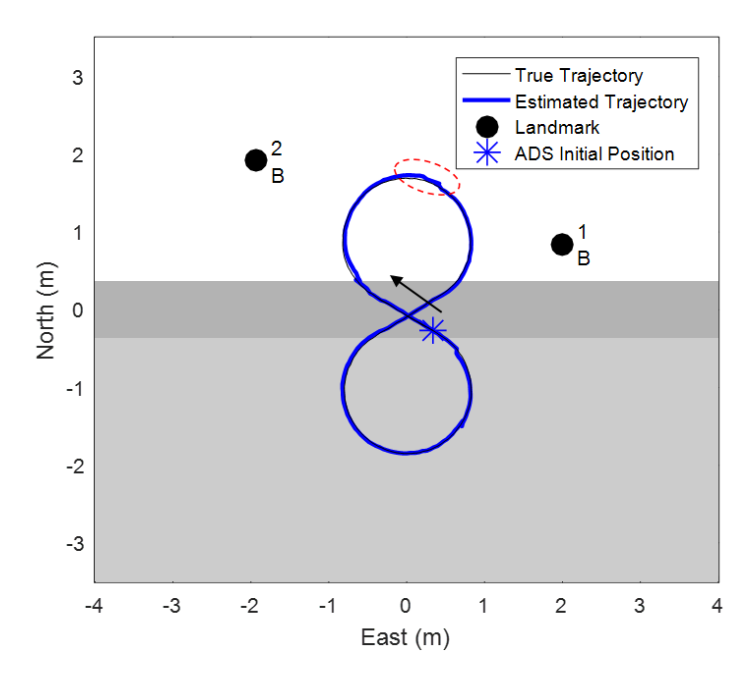
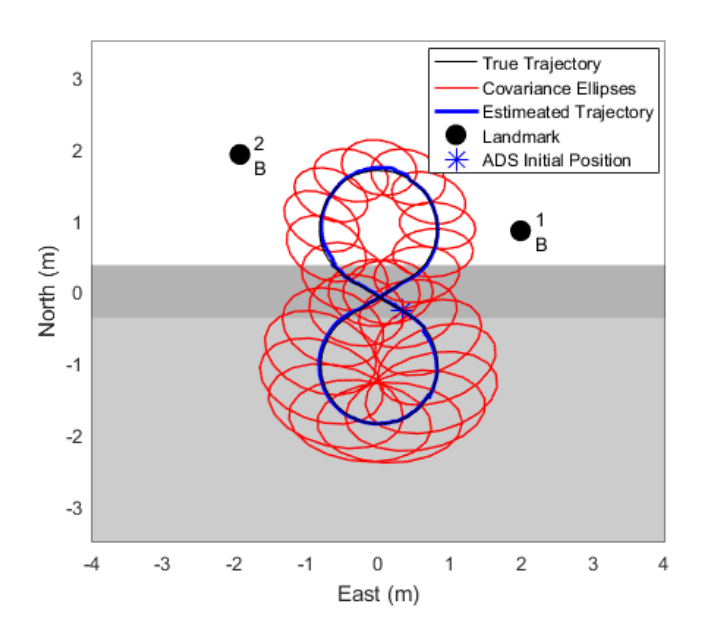


Figure 5. Landmark Geometry and True versus Estimated Vehicle Trajectory in Local Navigation Frame for Test 1

Figure 6 shows red covariance ellipses representing two-dimensional positioning uncertainty for ADS locations taken at regular 0.8 s intervals. Covariance ellipses are inflated by a factor 5 to facilitate visualization. We keep the positioning update interval and inflation factor the same for Tests 1 to 4.

Figure 7 represents the cross-track positioning error and covariance envelope (the '1- σ ' one-dimensional envelope represents the boundary within which 68% of the error samples are expected to lie, assuming zero mean error). In this case, the cross-track positioning error (thick curve) is within the covariance envelope (thin curves) at all times.



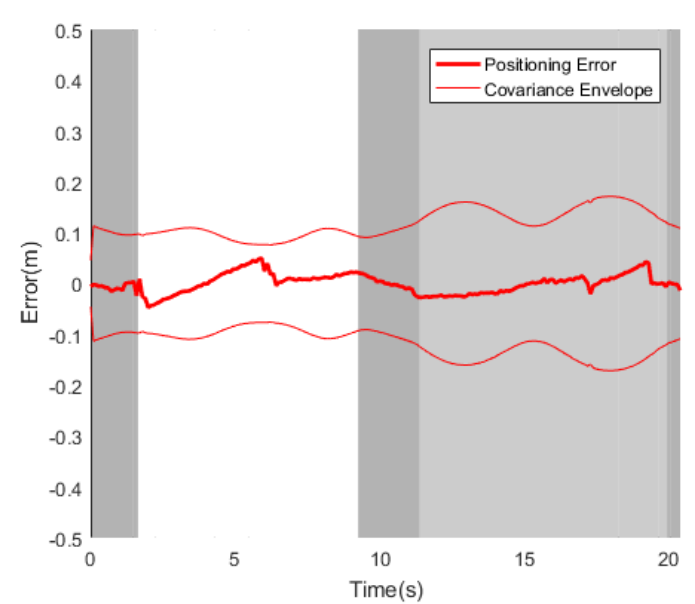
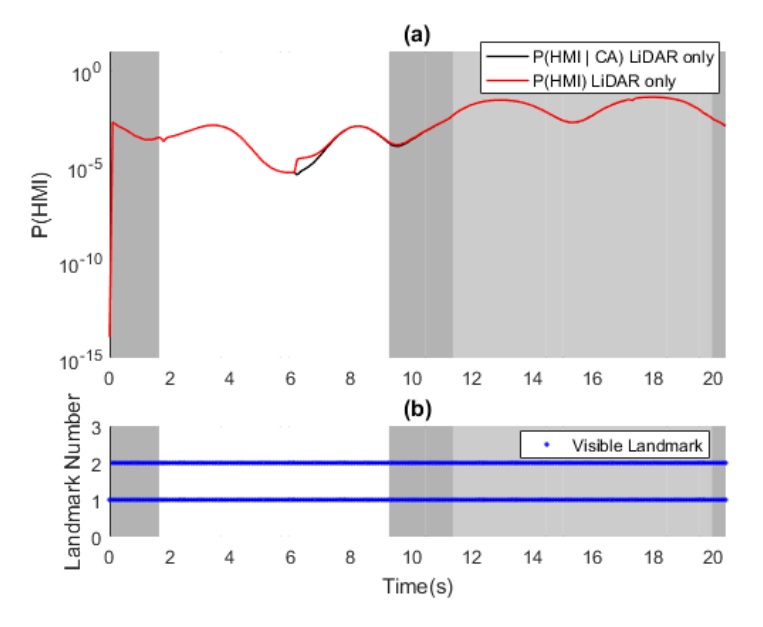


Figure 6. Covariance Ellipses at Multiple Time Steps for Test 1

Figure 7. Cross Track Positioning Error and Covariance Envelope Over Time for Test 1

Figure 8-(a) displays integrity risk bounds for the LiDAR-only implementation. The integrity risk bound is our estimate of the risk that the cross-track positioning error exceeds a 0.35 m alert limit (we assumed an example 0.35 m limit based on [30]). The black $P(HMI \mid CA)$ -curve assumes correct data association at all time steps and is directly derived from the EKF variance [15]. The red P(HMI) -curve accounts for potential incorrect associations at past or current times. Figure 8-(b) shows that landmarks 1 and 2 are continuously observed and extracted by the LiDAR. Even though, in this particular run, the landmarks are correctly associated (if not, we would see large, abrupt changes of the thick curve in Figure 7) we can only ensure that the risk of incorrect association is between 10^{-6} and 10^{-2} .

In Figure 8 (a), the red and black curves overlap through most of the trajectory, except for a short time interval between Times 6 s and 8 s. To better understand this discrepency, the corresponding segment of the trajectory is circled in a red dashed ellipse in Figure 5. At this location, the rover and the two landmarks are almost aligned. In parallel, Figure 9 shows the perceived *separation* between landmarks, i.e., the weighted innovation vector's norm (γ) when landmarks 1 and 2 are incorrectly associated. For small γ -values, correct and incorrect associations become difficult to distinguish, which increases the risk of incorrect association and hence increases the P(HMI)-bound. In this LiDAR-only test where the rover kinematic model is unreliable, and at this point in the trajectory where landmarks and vehicle are aligned, the navigation system does not have enough information to guarantee that the vehicle is either facing East or West. Additional information from an IMU addresses this problem, and can even help coast through periods of lack of LiDAR data.



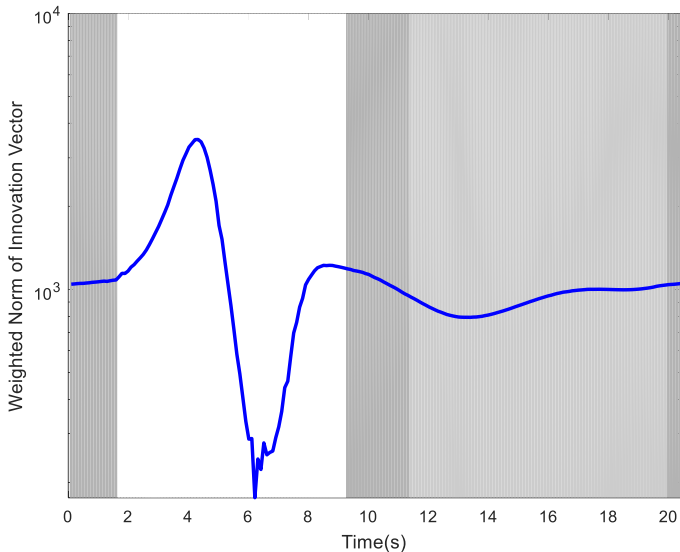


Figure 8. For Test 1: (a) Integrity Risk Bounds Assuming Correct Associations Versus Accounting for Incorrect Associations; (b)

Landmark Visibility

Figure 9. For Test 1: Weighted Norm of Innovation Vector for Incorrectly Associating Landmarks 1 and 2 (also referred to as 'Separation' between Landmarks 1 and 2)

5.2 Using IMU and LiDAR with Limited Range

In Test 2, we consider two sensor configurations: LiDAR-only and IMU/LiDAR. IMU parameter values are listed in Table 4. To evaluate the IMU's ability to coast through periods of LiDAR data unavailability, we artificially impose a four meter LiDAR range limit. This limit causes Landmark 2 to become unobservable for a segment of the trajectory, where only Landmark 1 is visible.

Table 4. IMU Parameter Values

System Parameters	Values
Accelerometer Power Spectral Density	$0.079~\text{m/s}^2/\sqrt{\text{Hz}}$
Gyroscope Power Spectral Density	$0.005 \text{ rad/}\sqrt{\text{s}}$
Accelerometer GMP Bias Correlation Time Constant	3600 s
Gyroscope GMP Bias Correlation Time Constant	3600 s
Standard Deviation of Accelerometer GMP Bias	0.67 m/s^2
Standard Deviation of Gyroscope GMP Bias	10 deg
IMU Sampling Time	0.01 s

Figure 10 shows the ADS true and estimated trajectories for LiDAR-only in Figure 10-(a) and for IMU/LiDAR in Figure 10-(b). The red segment of the estimated trajectory indicates where Landmark 2 is out of view. As compared to Figure 10-(a), Figure 10-(b) shows that integrating IMU measurements helps maintain low trajectory tracking errors.

Figure 11 (a) shows LiDAR-only covariance ellipses, which are fairly small when both landmarks are in view, but increase dramatically when Landmark 2 is out of view. It is worth noting that this is not an integrity issue because we have a clear indication of poor localization performance. But, it is an availability or continuity issue: we would not use the system in such a high risk situation. In contrast, in Figure 11 (b), IMU/LiDAR covariance ellipses are smaller than for LiDAR-only throughout the trajectory, and do not increase greatly when Landmark 2 is out of view.

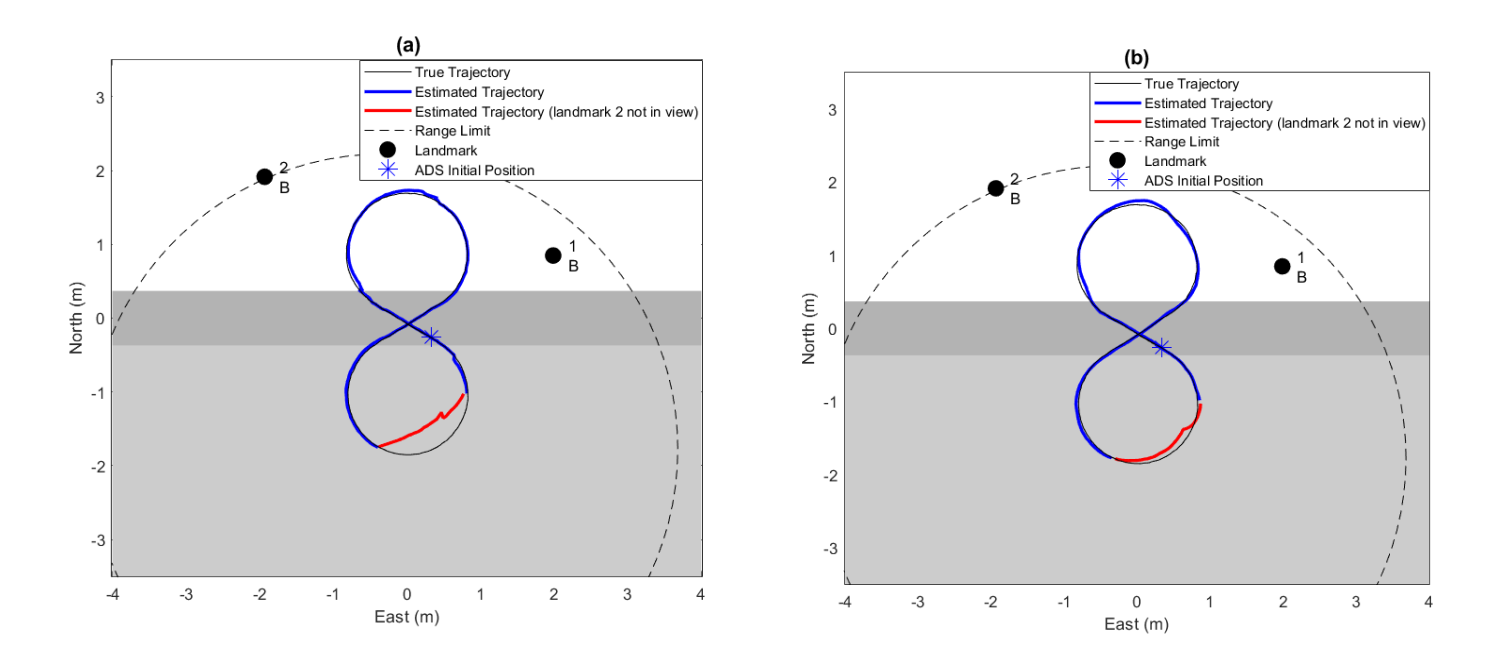


Figure 10. For Test 2: Estimated Vehicle Trajectory Assuming a 4-meter LiDAR Range Limit Using
(a) LiDAR-Only (b) IMU/LiDAR

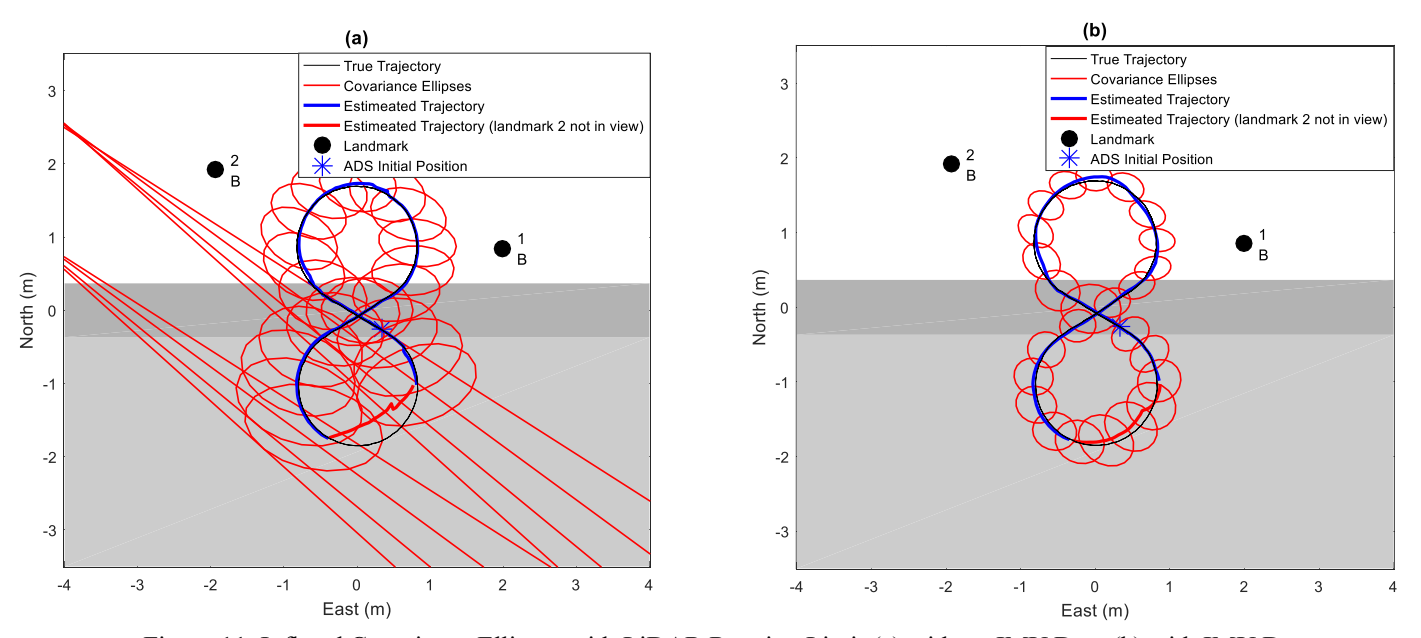


Figure 11. Inflated Covariance Ellipses with LiDAR Ranging Limit (a) without IMU Data (b) with IMU Data

Figure 12(a) and (b) respectively show integrity risk bounds and landmark availability over time. In Figure 12 (a), the black curves are $P(HMI \mid CA)$ -curves, and red is used to represent P(HMI); thin lines are used for LiDAR-only and thick lines for IMU/LiDAR. When Landmark 2 gets out of view, the P(HMI) and $P(HMI \mid CA)$ bounds for LiDAR-only approach one. $P(HMI \mid CA)$ decreases again when Landmark 2 comes back in view, but P(HMI) stays high because past time associations can still impact current-time integrity risk. The red and black IMU/LiDAR risk curves overlap and remain orders of magnitude lower thank LiDAR-only, showing that IMU not only improves estimation performance, but also reduces the risk of incorrect associations.

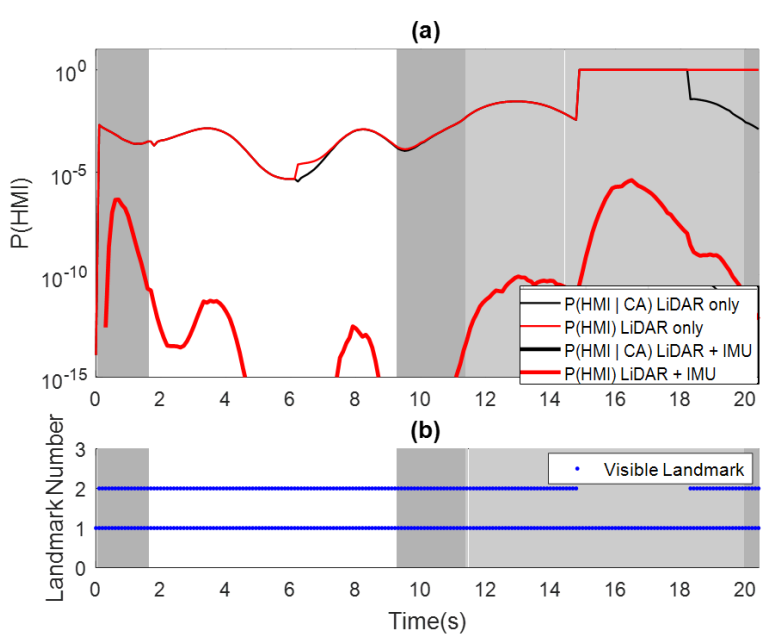


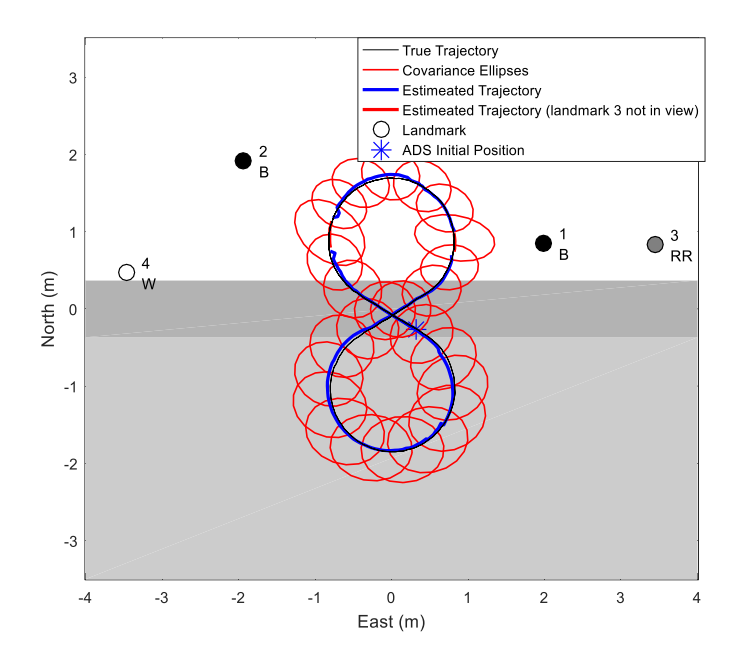
Figure 12. For Test 2: (a) Integrity Risk Bounds Assuming a 4-Meter LiDAR Range Limit Using LiDAR-Only versus IMU/LiDAR; (b) Landmark Visibility

5.3 Using LiDAR Range, Bearing Angles and Return-Light Intensity

In Test 3, we do not use the IMU, but use LiDAR range, bearing angle, and return light intensity measurements. We label this sensor configuration LiDAR+. LiDAR intensity measurements are used to improve data association. In this test, we place four landmarks with different surface reflectivities around the vehicle path. The surface of Landmarks 1 and 2 is black, that of Landmark 4 is white, and that of Landmark 3 is covered with retro-reflective tape. In this preliminary work, we compare the mean measured intensity over all data points associated with a landmark to the mean intensities stored in the map. This helps distinguish landmarks from each other and therefore improves data association.

In addition, as illustrated in Figure 13, Landmark 3 gets occluded by Landmark 1 for a few rover locations in the upper-loop of the figure eight. This arrangement makes data association more challenging because Landmarks 1 and 3 appear close to each other for certain rover locations.

In Figure 13, the red segments represent ADS locations where Landmark 3 is hidden behind Landmark 1. Covariance ellipses are smaller than in Figure 6 because two additional landmarks are visible. Ellipses grow when Landmark 3 is hidden. LiDAR intensity measurements do not affect trajectory estimation



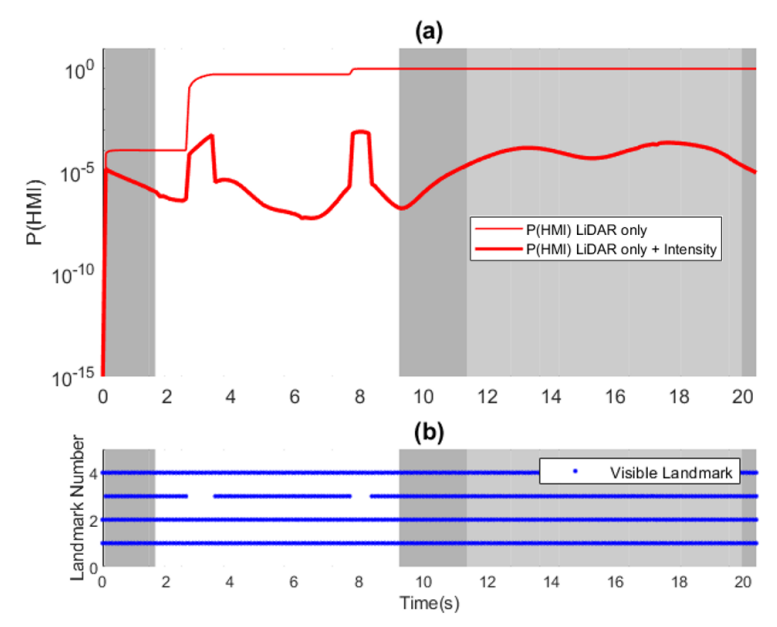


Figure 13. For Test 3: Positioning Covariance Ellipses Using LiDAR+Intensity

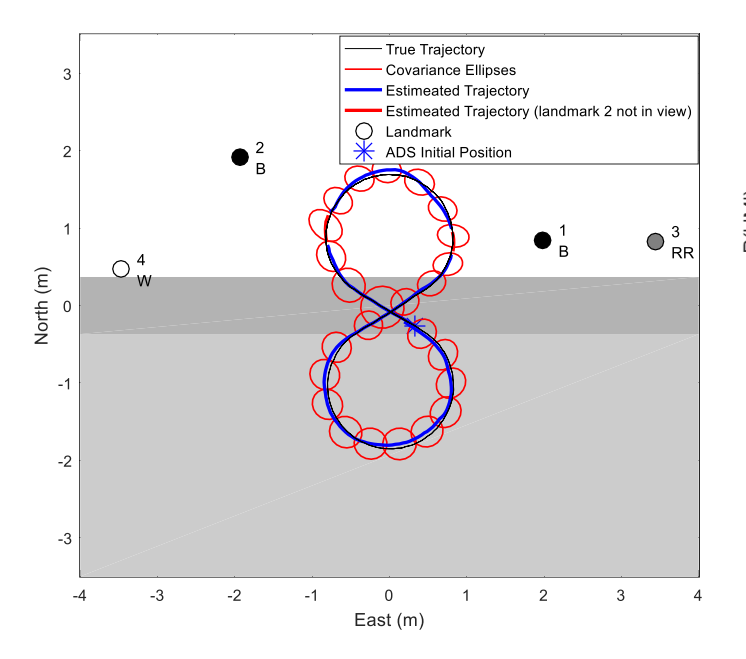
Figure 14. For Test 3: (a) Integrity Risk Bounds Using LiDAR-Only versus LiDAR+Intensity; (b) Landmark Visibility

Figure 14 (a) shows P(HMI)-curves for LiDAR-only (thin curve), and LiDAR+ (thick curve). Figure 14 (b) displays the landmark availability. The thin LiDAR-only curve suddenly increases at time '3 s', which is the time when Landmark 3 first gets occluded by Landmark 1. In contrast, low risk levels are maintained using LiDAR+ because intensity measurements help correctly identify landmarks.

5.4 Using LiDAR Range, Bearing, Intensity and IMU

In Test 4, we integrate IMU with LiDAR range, bearing and intensity measurements, which we refer to as the 'IMU/LiDAR+' configuration. We use the same landmarks as in Test 3. Figure 15 shows that the ADS positioning covariance ellipses are much smaller using IMU/LiDAR+ than using LiDAR+ in Figure 13.

Figure 16 confirms these observation by showing P(HMI) curves for IMU/LiDAR and IMU/LiDAR+, as well as for LiDAR-only and LiDAR+. LiDAR-only performs relatively poorly in this test, with the P(HMI)-bound approaching 1 as soon as the first difficult-to-identify landmark geometry is encountered. IMU/LiDAR performs better at the beginning, but the P(HMI)-bound still approaches 1 after first difficult-to-dinstinguish landmarks. LiDAR+ is consistently better, except when Landmark 3 gets occluded causing poorer estimation performance because fewer measurements are available. Finally, IMU/LiDAR+ expectedly outperforms all other configurations, and our tests show that the resulting P(HMI)-bound is at least four orders of magnitude lower than in the other cases, remaining below 10^{-10} throughout the test.



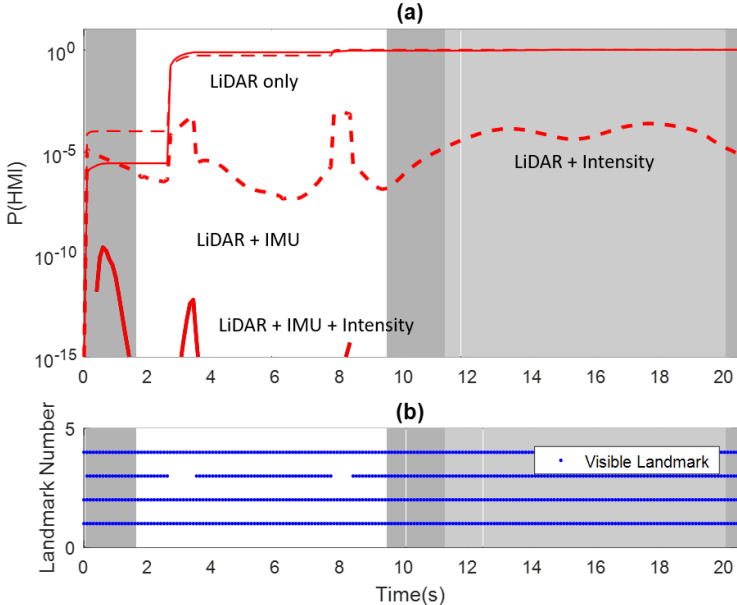


Figure 15. <u>For Test 4:</u> Covariance Ellipses Using IMU/LiDAR+Intensity

Figure 16. For Test 4: (a) Integrity Risk Bounds Using LiDAR-Only Versus LiDAR+, IMU/LiDAR, IMU/LiDAR +Intensity; (b) LiDAR's Landmark Visibility

6. Conclusion

In this paper, we derived a new IMU/LiDAR integration method that enables integrity risk evaluation while accounting for all possible incorrect associations between observed and mapped landmarks. Our method also incorporates LiDAR returnlight intensity measurements to better distinguish landmarks, thereby increasing the probability of correct association P(CA). We implemented a new analytical method to quantify the improvement in P(CA). In addition, we developed a testbed to evaluate our method with empirical data in a structured, well-understood environment. Four different configurations were tested. The four configurations were used to quantify and analyze the P(CA)-improvement provided by IMU data and LiDAR intensity measurements as compared to using LiDAR-only. The performance assessment shows a reduction in integrity risk of several orders of magnitude brought by IMU and LiDAR intensity in our selected testing environment. Future work includes tesing these methods in more realistic, unstructured environments, evaluating multi-sensor integrity risk over repeated trajectories and using more sofisticated methods for feature extraction.

Appendix A - Linearized IMU and LiDAR Measurement Equations Coefficients

In this appendix, we describe the coefficient matrices used in equations (3) and (12).

The coefficient matrix used in equation (3) is:

$$\mathbf{B}_{\phi,\theta,\psi} = \begin{bmatrix} -\sin(\psi)\cos(\theta) & \cos(\psi) & 0\\ \sin(\theta) & 0 & 1\\ \cos(\psi)\cos(\theta) & \sin(\psi) & 0 \end{bmatrix}^{-1}$$
(A.1)

The coefficient martrices corresponding to IMU measurements in equation (12) can be defined as [23]:

$$\mathbf{F}_{V2T} = \begin{bmatrix} 0 & \frac{1}{R+h} & 0\\ \frac{1}{R+h} & 0 & 0\\ 0 & \frac{-\tan(\lambda)}{R+h} & 0 \end{bmatrix}$$
(A.2)

$$\mathbf{F}_{H2V} = \begin{bmatrix} 0 & -\frac{2g_0}{R} & 0\\ \frac{2g_0}{R} & 0 & 0\\ 0 & 0 & 0 \end{bmatrix}$$
 (A.3)

where

R is the earth radius

h is the vehicle altitude

 λ is the vehicle latitude

 g_0 is the acceleration of gravity at zero altitude

The coefficients matrices corresponding to LiDAR measurements in equations (21) are [7]:

$$\mathbf{F}_{d,x} = \begin{bmatrix} -\frac{1}{\|\mathbf{p}_{E} - \mathbf{x}_{E}} & \cdots & -\frac{\mathbf{n}_{L}}{\|\mathbf{n}_{L}} \mathbf{p}_{E} - \mathbf{x}_{E}} \\ -\frac{1}{\|\mathbf{p}_{N} - \mathbf{x}_{N}} & \cdots & -\frac{\mathbf{n}_{L}}{\|\mathbf{n}_{L}} \mathbf{p}_{E} - \mathbf{x}_{E}} \\ 0 & \cdots & 0 \end{bmatrix}^{T}$$

$$(A.4)$$

$$\mathbf{F}_{\theta,x} = \begin{bmatrix} \frac{1}{\|\mathbf{p}_{N} - \mathbf{x}_{N}\|^{2}} & \cdots & \frac{\mathbf{n}_{L}}{\|\mathbf{n}_{L}} \mathbf{p}_{N} - \mathbf{x}_{N} \\ \frac{1}{\|\mathbf{p}_{L}} \mathbf{p}_{N} - \mathbf{x}_{N} \|^{2} \\ -\frac{1}{\|\mathbf{p}_{L}} \mathbf{p}_{N} - \mathbf{x}_{N} \|^{2} & \cdots & -\frac{\mathbf{n}_{L}}{\|\mathbf{n}_{L}} \mathbf{p}_{N} - \mathbf{x}_{N} \|^{2} \\ 0 & \cdots & 0 \end{bmatrix}^{T}$$
(A.5)

Where $\overline{\mathbf{x}}_{EN} = \begin{bmatrix} x_E & x_N \end{bmatrix}^T$ (also apering in ADS position states equation (14)) and $\mathbf{P} = \begin{bmatrix} P_E & P_N \end{bmatrix}^T$

$$\mathbf{F}_{\theta,e} = \begin{bmatrix} 0 & 0 & 1 \\ & \vdots & \\ 0 & 0 & 1 \end{bmatrix}_{n,x3} \tag{A.6}$$

Appendix B - Discrete-Time Equations of IMU

We use the Van Loan algorithm to determine the discrete-time state propagation matrix Φ_k based on the continuous-time matrices \mathbf{F} and \mathbf{w} [27]. The following equations are the discrete-time form of equations (4, 5, 7, 8)

$${}^{\mathrm{B}}\tilde{\boldsymbol{\omega}}_{k}^{\mathrm{IB}} = \left[\mathbf{I} + \mathbf{S}_{\sigma} + \mathbf{M}_{\sigma}\right] {}^{\mathrm{B}}\boldsymbol{\omega}_{k}^{\mathrm{IB}} + \mathbf{b}_{\sigma k} + \mathbf{v}_{\sigma k} \tag{B.1}$$

$${}^{\mathrm{B}}\bar{\boldsymbol{\omega}}_{k}^{\mathrm{IB}} = [\mathbf{I} + \hat{\mathbf{S}}_{g} + \hat{\mathbf{M}}_{g}]^{-1} ({}^{\mathrm{B}}\tilde{\boldsymbol{\omega}}_{k}^{\mathrm{IB}} - \hat{\mathbf{b}}_{g,k})$$
(B.2)

$${}^{\mathrm{B}}\tilde{\mathbf{f}}_{k}^{\mathrm{I}} = [\mathbf{I} + \mathbf{S}_{a} + \mathbf{M}_{a}] {}^{\mathrm{B}}\mathbf{f}_{k}^{\mathrm{I}} + \mathbf{b}_{ak} + \mathbf{v}_{ak}$$
(B.3)

$${}^{\mathrm{B}}\overline{\mathbf{f}}_{k}^{\mathrm{I}} = [\mathbf{I} + \hat{\mathbf{S}}_{a} + \hat{\mathbf{M}}_{a}]^{-1} ({}^{\mathrm{B}}\widetilde{\mathbf{f}}_{k}^{\mathrm{I}} - \hat{\mathbf{b}}_{ak})$$
(B.4)

The following equations are the discrete-time form of equations (6) and (9)

$$\mathbf{b}_{g,k+1} = e^{-\frac{T_s}{\tau_g}} \mathbf{b}_{g,k} + \mathbf{n}_{a,k} \tag{B.5}$$

$$\mathbf{b}_{a,k+1} = e^{-\frac{T_s}{\tau_a}} \mathbf{b}_{a,k} + \mathbf{n}_{a,k}$$
(B.6)

Appendix C - Overbounding of Measurement Error Distributions

This appendix outlines the method that we used to derive a probabilistic model for the extracted feature measurements. This method is based on over-bounding theory [4, 5]. We collected LiDAR point cloud data for 4250 of sensor-to-landmark geometries (landmarks are vertical cylinders), processed them using our feature extractor, and stored the estimated point-feature range and bearing angle measurements.

Figures C.1 and C.2 respectively show the range and bearing angle measurement error cumulative distribution functions (CDF) on quantile to quantile plots. On these plots, the x-axis is the theoretical standard normal distribution quantiles and the y-axis is the sample measurement error distribution quantiles. If the empirical measurement error distribution were a normal distribution, the sample points would align along a straight line with slope the sample standard deviation, and y-intercept the sample mean. Figures C.1 and C.2 show that the core of the distribution behave like a normal distribution within \pm 2 sigmas, i.e., 95% of the time. But the sample distributions have wide tails.

We leverage overbounding theory, which is used in aviation navigation, to model these complicated sample distributions [4, 5, 31]. The black lines in Figures C.1 and C.2 are overbounding Gaussian functions. Their standard deviations are 0.12 meter for the range measurement error (versus 0.03 m for the sample distribution), and 2 degrees for the bearing angle measurement error (versus 1 deg for the sample distribution).

Figure C.1 Range Measurement Error Distribution and Overbounding Gaussian Model

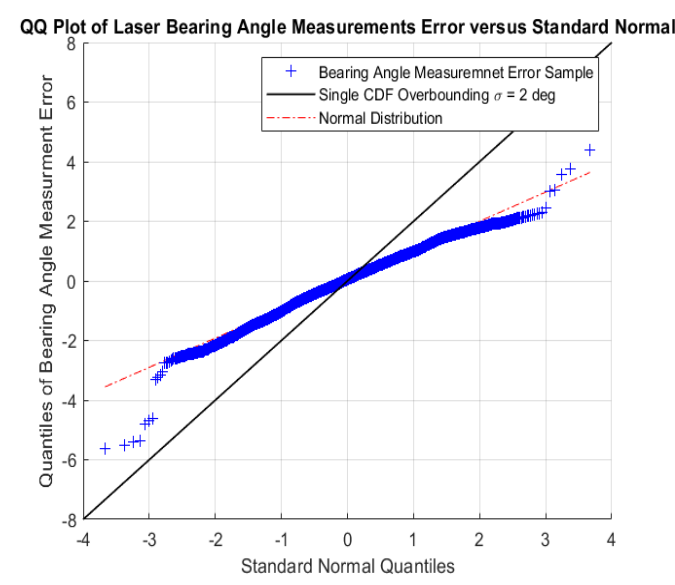


Figure C.2 Bearing Angle Measurement Error Distribution and Overbounding Gaussian Model

ACKNOWLEDGMENTS

The authors gratefully acknowledge the National Science Foundation for supporting this research (NSF award CMMI-1637899). However, the opinions expressed in this paper do not necessarily represent those of any other organization or person.

References

- [1] RTCA Special Committee 159, "Minimum Operational Performance Standards for Global Positioning System/Wide Area Augmentation System Airborne Equipment," *RTCA/DO-229C Standard*, 2001, pp. 1–21.
- [2] Lee, Y.C. "Analysis of range and position comparison methods as a means to provide GPS integrity in the user receiver" *Proc. 42nd Annu. Meet. Inst. Navig., Seattle, WA, USA, 1986, pp. 1–4.*
- [3] Parkinson, B.W, Axelrad, P. "Autonomous GPS integrity monitoring using the pseudorange residual" *NAVIGATION*, vol. 35, no. 2, 1988, pp. 225–274.
- [4] DeCleene, B. "Defining Pseudorange Integrity Overbounding," *Proc. ION GPS 2000, Salt Lake City, UT., 2000, pp. 1916-1924.*
- [5] Rife, J., Pullen, S., Enge, P. and Pervan, B. "Paired Overbounding for Nonideal LAAS and WAAS Error Distributions." *IEEE TAES, Vol. 42, No. 4, 2006 pp. 1386-1395*.
- [6] Joerger, M., B. Pervan. "Measurement-Level Integration of Carrier-Phase GPS and Laser-Scanner for Outdoor Ground Vehicle Navigation." ASME Journal of Dynamic Systems, Measurement, and Control. 131. 2009.
- [7] Joerger, M. "Carrier Phase GPS Augmentation Using Laser Scanners and Using Low Earth Orbiting Satellites," *Ph.D. Dissertation, Illinois Institute of Technology, 2009.*
- [8] Bailey, T. "Mobile Robot Localisation and Mapping in Extensive Outdoor Environments," *PhD Dissertation, The University of Sydney, 2002.*
- [9] Cooper, A.J. "A Comparison of Data Association Techniques for Simultaneous Localization and Mapping," M.S. Thesis, Massachussetts Institute of Technology, 2005.
- [10] Tena Ruiz, I., Petillot, Y., Lane, D. M. and Salson, C. "Feature Extraction and Data Association for AUV Concurrent Mapping and Localisation," *Proc. IEEE-ICRA*, 2001.
- [11] Nguyen, V., Martinelli, A., Tomatis, N., and Siegwart, R. "A Comparison of Line Extraction Algorithms using 2D Laser Rangefinder for Indoor Mobile Robotics," *Proc. IEEE/RSJ IROS, 2005*.

- [12] Bar-Shalom, Y. and Fortmann, T. E. "Tracking and Data Association," *Mathematics in Science and Engineering, Vol.* 179. Academic Press. 1988.
- [13] Pfister, S. T., Kriechbaum, K. L., Roumeliotis, S. I., Burdick, J. W. "Weighted Range Sensor Matching Algorithms for Mobile Robot Displacement Estimation," *Proc IEEE ICRA*, 2002.
- [14] Thrun, S., Burgard, W. and Fox, D. "A Probabilistic Approach to Concurrent Mapping and Localization for Mobile Robots," *Machine Learning and Autonomous Robots, Vol. 31, No. 5, 1998, pp. 1-25.*
- [15] Hassani, Ali, Joerger, Mathieu, Arana, Guillermo Duenas, Spenko, Matthew, "LiDAR Data Association Risk Reduction Using Tight Integration with INS," *Proceedings of the 31st International Technical Meeting of the Satellite Division of The Institute of Navigation (ION GNSS+ 2018), Miami, Florida, September 2018, pp. 2467-2483.*
- [16] Joerger, M., Jamoom, M., Spenko, M. and Pervan, B. "Integrity of Laser-Based Feature Extraction and Data Association," *Proceedings of IEEE/ION PLANS 2016, Savannah, GA, April 2016, pp. 557-571.*
- [17] Joerger, M., Pervan, B. "Continuity Risk of Feature Extraction for Laser-Based Navigation," *Proceedings of the 2017 International Technical Meeting of The Institute of Navigation, Monterey, California, January 2017, pp. 839-855.*
- [18] Joerger, M., Arana Duenas, G., Spenko, M. and Pervan, B. "Landmark Data Selection and Unmapped Obstacle Detection in Lidar-Based Navigation," *Proceedings of the 30th International Technical Meeting of The Satellite Division of the Institute of Navigation (ION GNSS+ 2017), Portland, Oregon, September 2017, pp. 1886-1903.*
- [19] Duenas Arana, G., Joerger, M., and Spenko, M. "Minimizing Integrity Risk via Landmark Selection in Mobile Robot Localization." accepted for publication in *Proceedings of IEEE International Conference on Robotics and Automation (ICRA2018). Brisbane, Australia. 2018.*
- [20] Opromolla, R., Fasano, G., Rufino, G., Grassi, M. and Savvaris, A. "LIDAR-Inertial Integration for UAV Localization and Mapping in Complex Environment." *International Conference on Unmanned Aircraft Systems (ICUAS), 2016*
- [21] Soloviev, A., Bates, D. and Van Graas. F. "Tight Coupling of Laser Scanner and Inertial Measuring for Fully Autonomous Relative Navigation." *Navigation*, 54(3), pp.189-205, 2007
- [22] Soloviev. A. "Tight Coupling of GPS, Laser Scanner and Inertial Measuring for Navigation in Urban Environments." *IEEE/ION Position, Location and Navigation Symposium, 2008*
- [23] Titterton, D., Weston, J. "Strapdown inertial navigation technology." Stevenage: The Inst. of Engineering and Technology, 2009
- [24] Rogers, R. "Applied mathematics in integrated navigation systems." 3rd ed. Reston: American Institute of Aeronautics and Astronautics, 2007
- [25] Savage, P.G., "Strapdown Inertial Navigation Integration Algorithm Design Part 2: Velocity and Position Algorithms" Journal of Guidance, Control, and Dynamics Vol. 21, No. 2, March–April 1998
- [26] Savage, P.G., "Strapdown Inertial Navigation Integration Algorithm Design Part 1: Attitude Algorithms" *Journal of Guidance, Control, and Dynamics Vol. 21, No. 1, January–February 1998*
- [27] Brown, R. Hwang, P. "Introduction to Random Signals and Applied Kalman Filtering. Hoboken." NJ: John Wiley and Sons, 2012
- [28] Williams, S.B., Dissanayake, G. and Durrant-Whyte, H. "An efficient Approach to the Simultaneous Localisation and Mapping Problem," *Proc. IEEE-ICRA*, 2002
- [29] Joerger, M. Pervan, B. "Quantifying Safety of Laser-Based Navigation," in press. *IEEE Transactions on Aerospace and Electronic Systems*, 2018
- [30] Reid et al., "Localization Requirments for Autonomous Vehicles," https://arxiv.org/abs/1906.01061
- [31] Blanch et al., "Gaussian Bounds of Sample Distributions for Integrity Analysis," *IEEE Transactions on Aerospace and Electronic Systems*, vol. 55, no. 4, pp. 1806–1815, 2019